Chemical Science

ROYAL SOCIETY OF CHEMISTRY

EDGE ARTICLE

View Article Online
View Journal

Cite this: DOI: 10.1039/d6sc00877a

All publication charges for this article have been paid for by the Royal Society of Chemistry

Low-valent Mo single atoms stabilized by electronegative oxygen coordination enable efficient water oxidation

Yang Yang, *[a] Ji-Kai Li,[a] Qian-Nan Yang,[a] Yi-Bin Yang,*[b] Jian-Hua Meng,[a] Lin Zhang,[c] Ying-Dan Wu,[a] Ke-Xiang Wang,[a] Huan Chen,[a] Zhi-Yuan Jiang,[a] Rui Chao,[a] Wei-Tao Wang,[a] Xiao Ma*[c] and Zhao-Tie Liu *[ad]

Rational design and atomically precise synthesis of efficiently low-valent single atom catalysts, particularly those in which isolated transition-metal centers are directly coordinated to highly electronegative oxygen atoms embedded within layered double hydroxide (LDH) or oxyhydroxide matrices, are pivotal for surmounting the kinetic bottlenecks of the oxygen evolution reaction (OER). In the present work, low-valent molybdenum single atoms (Mo SAs) are successfully anchored onto NiFe LDH (^{LSA}Mo-NiFe LDH) through a low-temperature solution-phase reduction process, resulting in a unique unsaturated and electron-rich Mo–O_3 coordination configuration. Under identical mass loadings, ^{LSA}Mo-NiFe LDH outperforms both pristine NiFe LDH and commercial IrO_2 in alkaline media, delivering substantially higher intrinsic activity. The boost stems from robust electronic interactions between low-valent Mo SAs and the NiFe LDH lattice, which synergistically optimizes the local electronic structure. Remarkably, when architecturally engineered into a 3D monolithic electrode on nickel foam, this electrode achieves an ultra-low overpotential of 158 mV at 10 mA cm^{-2}, ranking it among the most active single-atom-based OER electrocatalysts yet reported. Post-characterization analyses corroborate that ^{LSA}Mo-NiFe LDH retains its atomic architecture and stoichiometry after prolonged operation. Importantly, *operando* electrochemical characterization further reveals that the lattice oxygen mechanism pathway serves as the primary redox partner during the OER. Theoretical calculations reveal that the low-valent Mo SAs enhance OER activity and identify the rate-determining steps in the OER process. The present work delivers a universal blueprint for high-performance, low-valent monoatomic catalysts: craft under-coordinated metal centers whose electron density is precisely modulated by adjacent, highly electronegative ligands.

Received 31st January 2026
Accepted 3rd March 2026

DOI: 10.1039/d6sc00877a

rsc.li/chemical-science

1 Introduction

The oxygen evolution reaction (OER), a kinetically sluggish process involving four coupled proton–electron transfers, is central to a lot of new kinds of clean-energy technologies and rechargeable batteries such as hydrogen fuel cells, water electrolyzers, and metal–air batteries.[1,2] This has intensified the quest for next-generation electrocatalysts that can accelerate OER kinetics by combining high activity and long-term stability. Currently, the scalable deployment of high-performance ruthenium- and iridium-oxide catalysts is hindered by their elemental scarcity and inadequate corrosion resistance.[3,4] The rational design and scalable synthesis of transition metal single-atom catalysts (SACs), which maximize atomic utilization efficiency, offers a highly effective approach to dramatically reduce or even completely eliminate the need for noble metals.[5] The OER activity of SACs is governed by both the density and intrinsic activity of their single-atom active sites (SAASs). While raising the metal loading increases site density, most high-loading SACs reported to date still demand substantial overpotentials (>200 mV) to deliver 10 mA cm^{-2}.[6,7] This is largely attributed to the relatively low intrinsic activity of each SAAS. According to the Sabatier principle, an ideal catalytic site of SACs should possess an optimal binding energy for adsorption and desorption of OER intermediates (*O, *OH, and *OOH).[8,9] To enhance the intrinsic activity of SAASs, the adsorption and desorption balance of OER intermediates must first be secured

[a]Key Laboratory of Chemical Additives for China National Light Industry, College of Chemistry and Chemical Engineering, Shaanxi University of Science and Technology, Xi'an, 710021, China. E-mail: yyang399@sust.edu.cn
[b]Chemical Pollution Control Chongqing Applied Technology Extension Center of Higher Vocational Colleges, Chongqing Industry Polytechnic University, Chongqing, 401120, China. E-mail: yangyb@cqipu.edu.cn
[c]State Key Laboratory of Solidification Processing, School of Materials Science and Engineering, Northwestern Polytechnical University, YouyiXi Road 127, Xi'an 710072, China. E-mail: maxiaonpu@nwpu.edu.cn
[d]School of Chemistry and Chemical Engineering, Shaanxi Normal University, Xi'an, 710119, China. E-mail: ztliu@snnu.edu.cn

by optimizing the electronic structure, which is largely determined by the intrinsic electronic configuration of the SAAS and its local coordination environment.[10,11] Therefore, concerted tailoring of both the electronic configuration and the coordination structure of SAASs is imperative to unlock the full intrinsic OER potential of transition metal SACs.

Among the burgeoning family of transition metal SACs, molybdenum SACs (Mo SACs) are attracting intensifying interest by virtue of their distinctive half-filled $4d^5 5s^1$ electronic configuration,[12] multiple oxidation states,[13] pronounced oxygen affinity,[14] and high intrinsic activity.[15] Many cutting-edge research studies are directed at increasing the valence state of Mo single atoms (Mo SAs) to enhance the inherent OER activity of Mo SACs.[16–18] However, the OER activity and stability of high valent Mo SAs are still severely limited to thermodynamic instability, gloomy electron cloud density, and less d-orbital electrons,[19–21] which are linked mainly to the influence of the electron structure and valence state of Mo SAs caused by the highly electronegative coordination atom of oxygen. A challenging solution may be to create low valent Mo SAs directly coordinated with oxygen instead of traditional less-electronegative atoms (*e.g.*, C, N, and S), which exhibit higher intrinsic activity and stability than the high valent Mo SAs for the OER. The solution rationale includes: (i) the differences of electronic structure and affinity of various transition metals create different coordination environments that lead to the difference of oxygen electronegativity in oxygen-containing transition metal supports;[22,23] (ii) oxygen atoms with relatively weaker electronegativity are favorable for strengthening the metal–oxygen covalency, which can lead to electron transfer from the lattice oxygen to the metal, and then reduce the oxidation state of the metal and promote the formation of low valent metal SAs in the oxygen-containing carriers;[24–26] (iii) oxygen atoms with unsaturated coordination, generally located at the defect, edge, and corner, have lower negativity than the saturated ones.[27–29] Accordingly, developing oxygen-containing transition metal supports with unsaturated-coordination oxygen sites to reduce the valence state of Mo SAs is the focus of synthesizing high-performance low valence Mo SACs for the OER.

Here, we report oxygen-stabilized low valent Mo SAs doped on an NiFe layered double hydroxide (LDH) support with abundant unsaturated oxygen sites (^{LSA}Mo-NiFe LDH) *via* a simple solvothermal reduction process. The quantitative analysis of the Fourier-transform extended X-ray absorption fine structure (FT-EXAFS) spectra verifies that the ^{LSA}Mo-NiFe LDH catalyst involves an unsaturated electron-rich Mo–O_3 motif that suppresses the Mo valence to a state below that in MoO_2. Importantly, RRDE tests conducted at identical mass loadings show that ^{LSA}Mo-NiFe LDH outperforms both the bare NiFe LDH support and commercial IrO_2 in the OER activity while maintaining a Faradaic efficiency (FE) of 99.5%. To fully exploit the OER potential of the catalyst, we directly grew ^{LSA}Mo-NiFe LDH on conductive nickel foam (^{LSA}Mo-NiFe LDH@NF) that demands only 158 mV to reach 10 mA cm^{-2} and exhibits a Tafel slope of 42.8 mV dec^{-1} in basic solution. *Ex-situ* analyses after prolonged OER operation corroborate the robust structural and elemental integrity of ^{LSA}Mo-NiFe LDH. Furthermore, *operando* attenuated total reflectance surface-enhanced infrared absorption spectroscopy (ATR-SEIRAS) and differential electrochemical mass spectrometry (DEMS) analyses reveal that the OER on ^{LSA}Mo-NiFe LDH proceeds *via* a lattice oxygen mechanism (LOM) pathway. DFT + *U* simulations reveal that low-valent Mo SAs optimize OH^- adsorption energy, activate lattice oxygen, and promote lattice oxygen vacancy formation, jointly lowering the energy barrier of the OER rate-determining steps. This study establishes a versatile strategy for crafting high-performance, low valent Mo SACs by utilizing Mo–O bonds to under-coordinated, electron-rich oxygen sites within the NiFe LDH support.

2 Results and discussion

The ^{LSA}Mo-NiFe LDH electrocatalyst was synthesized *via* a sequential hydrothermal and solvothermal protocol (Fig. 1a). First, NiFe LDH was prepared by a one-step hydrothermal reaction using nickel nitrate hexahydrate, ferrous chloride tetrahydrate and ammonium fluoride in the presence of urea as the precipitant. The powder X-ray diffraction (PXRD) pattern presented in Fig. S1 more closely matches that of the standard LDH structure (JCPDS # 40-0215) and confirms its high crystallinity.[30] Fourier-transform infrared spectroscopy (FT-IR) shows the stretching and bending vibrations of O–H (3425 cm^{-1}) and CO_3^{2-} anions (1359 and 800 cm^{-1}), indicating the existence of H_2O molecules and CO_3^{2-} anions in the interlaminations of NiFe LDH.[31] The Raman spectrum exhibits a broad peak (494-579 cm^{-1}) and a narrow peak (669 cm^{-1}), corresponding to metal–oxygen bonds (M–O, M = Ni and Fe) and CO_3^{2-} anions, respectively. Scanning electron microscopy (SEM) images reveal the presence of nanoparticles with varied sizes. The high-resolution transmission electron microscopy (HRTEM) image reveals distinct lattice fringes with a spacing of 0.237 nm, and the selected area electron diffraction (SAED) pattern displays two diffraction rings at (012) and (110), which are consistent with the peaks at 34.4 and 59.9° in the PXRD pattern, respectively. High-angle annular dark field-scanning transmission electron microscopy (HAADF-STEM) imaging and corresponding elemental mapping confirm the homogeneous distribution of Ni and Fe across the NiFe LDH. All of these physical characterization studies demonstrate the successful synthesis of the NiFe LDH support. Subsequently, Na_2MoO_4 was dissolved in NaOH solution and heated at 120 °C for 1 h in the presence of $NaBH_4$ solution and NiFe LDH support to prepare the ^{LSA}Mo-NiFe LDH target electrocatalyst. Here, $NaBH_4$ serves as a reductant to decrease the valence of the hexavalent Mo source in the formation of low valent Mo SAs. As shown in Fig. 1a, the reductive treatment drives Mo SAs to the edges of NiFe LDH, where they adopt an unsaturated Mo–O_3 coordination structure. The HRTEM images (Fig. 1b and S2) resolve three sets of lattice fringes in the ^{LSA}Mo-NiFe LDH sample, with the spacing of 0.265, 0.223, and 0.198 nm, corresponding to the (101), (015), and (018) planes. The SAED pattern (Fig. 1b, inset) exhibits (110) and (101) rings, and the HRTEM analysis collectively confirm the crystalline nature of the ^{LSA}Mo-NiFe LDH material. This suggests that many high-index planes

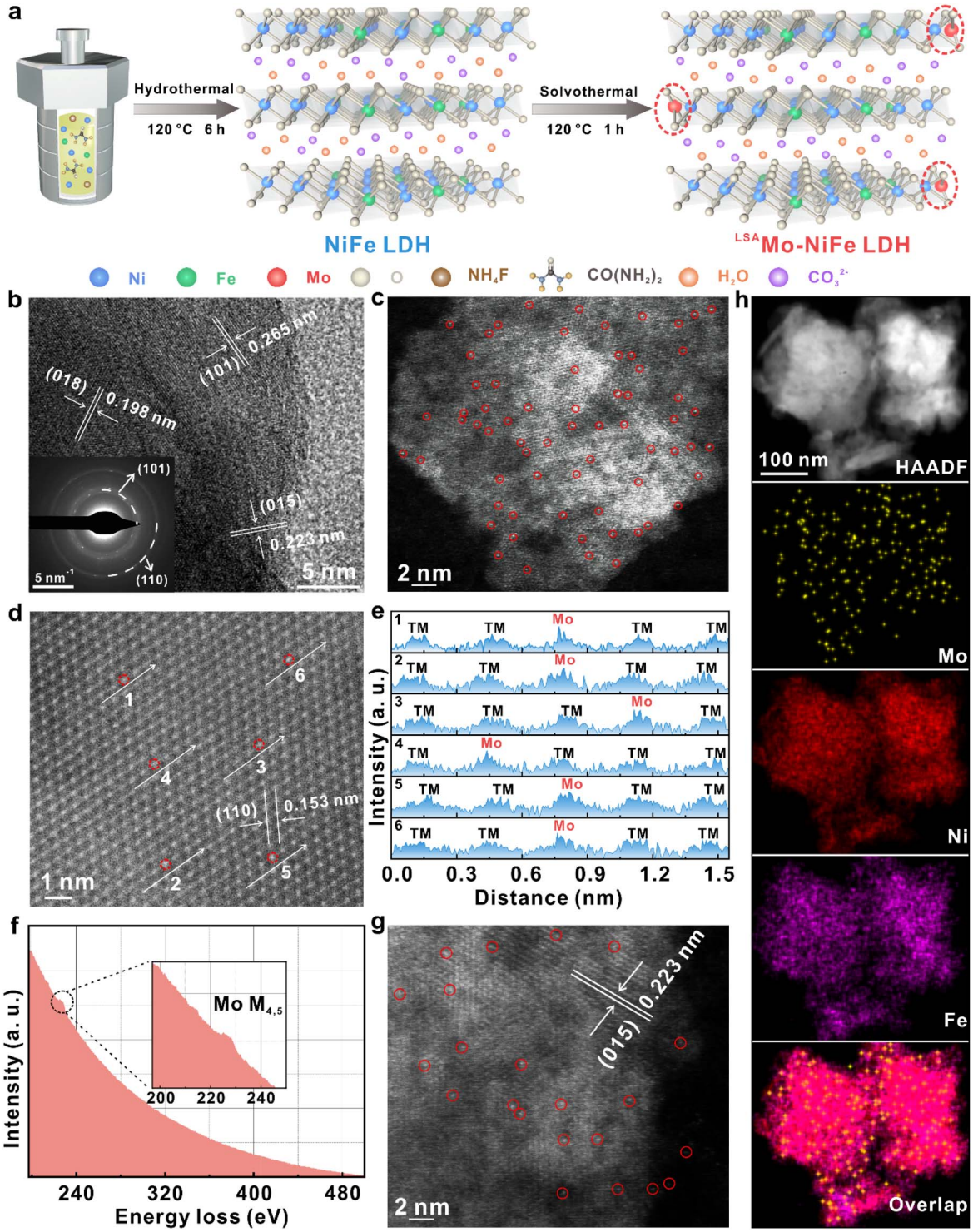

Fig. 1 Synthesis protocol and structural characterization of ^{LSA}Mo-NiFe LDH powder. (a) Schematic flow of catalyst synthesis. (b) HRTEM image and SAED pattern. (c) The spherical aberration-corrected HAADF-STEM image. (d) Atomic-resolution HAADF-STEM image. (e) Intensity profile of the single site in Fig. 1d; TM refers to Ni and Fe. (f) EELS spectrum. (g) The spherical aberration-corrected HAADF-STEM image. (h) Elemental mappings of Ni, Fe, and Mo in ^{LSA}Mo-NiFe LDH, respectively. Mo SAs are circled with red rings.

such as (015) and (018) are fully exposed on the ^{LSA}Mo-NiFe LDH sample, which are mostly attributed to the role of fluorine in significantly decreasing the surface free energy and inducing isotropic growth along the high-index facet orientation.[32,33] The above analyses also confirm the absence of aggregated metallic Mo nanoclusters or nanoparticles, ruling out the formation of large Mo species.

To verify the existence of Mo SAs at the atomic scale, spherical aberration-corrected HAADF-STEM was performed on the ^{LSA}Mo-NiFe LDH sample. Fig. 1c and d present the isolated

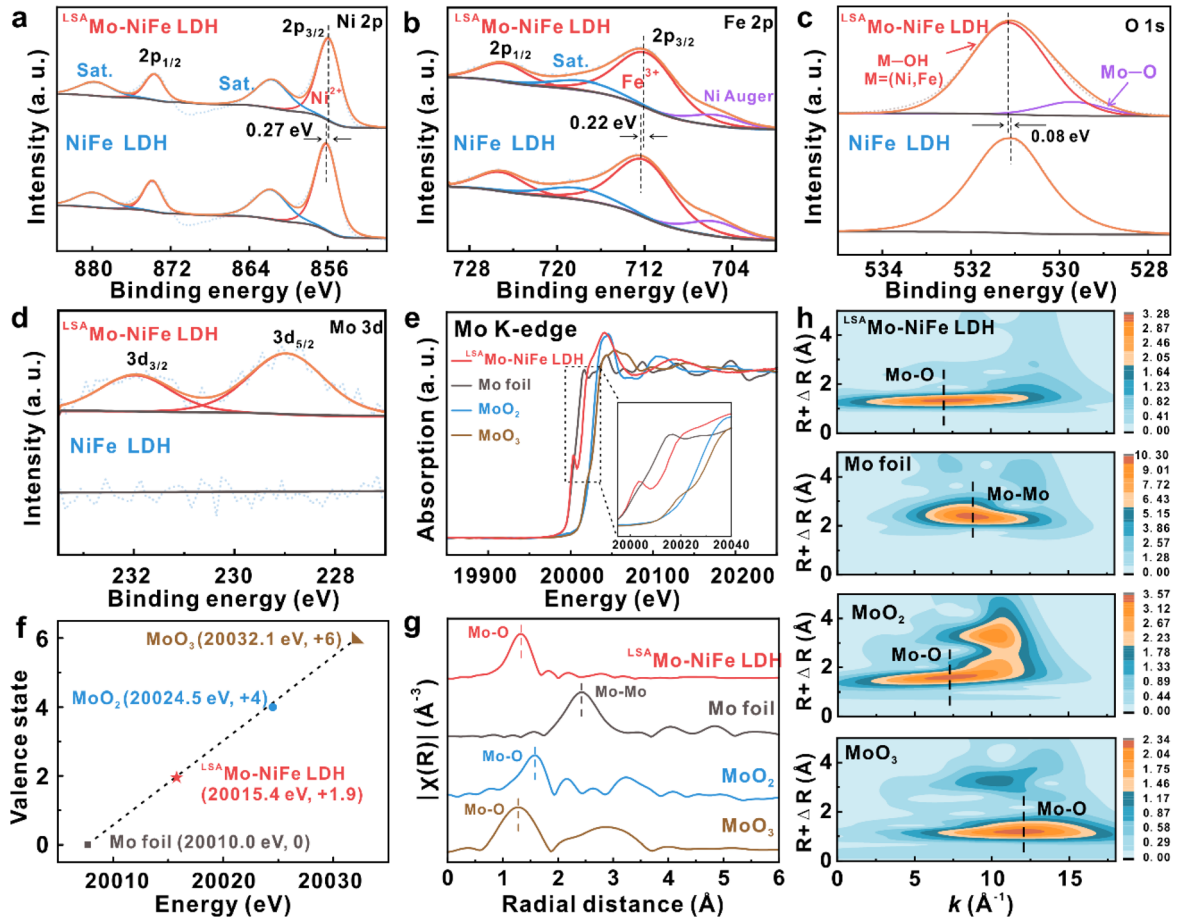

Fig. 2 Fine structural and electronic characterization of the LSAMo-NiFe LDH catalyst. (a–d) High-resolution XPS spectra of (a) Ni 2p, (b) Fe 2p, (c) O 1s, and (d) Mo 3d regions for the LSAMo-NiFe LDH and pristine NiFe LDH powders. (e) Normalized Mo K-edge XANES spectra of LSAMo-NiFe LDH and reference compounds. (f) Corresponding average oxidation states of Mo species. (g) Fourier-transform Mo K-edge EXAFS spectra. (h) Wavelet-transform EXAFS signals for LSAMo-NiFe LDH and reference samples.

bright spots circled in red and ordered matrix of Ni and Fe atoms along the [110] crystal orientation. The brighter lattice points in various atomic columns with six arrows can be identified as Mo SAs because of the higher atomic number (Z) of Mo relative to Ni and Fe. The undistinguished brightness between Ni and Fe lattice points is mainly due to the Z values that are very closely related. According to the Rutherford scattering theory, the intensity of electron–nucleus interactions scales with the square of the atomic number;[34,35] Mo atoms with a bigger Z show higher intensity than the surrounding Ni and Fe atoms (Fig. 1e). Importantly, the high-resolution electron energy loss spectroscopy (EELS) exhibits a weak $M_{4,5}$ signal of Mo atoms, verifying the existence of low-density Mo SAs in the LSAMo-NiFe LDH sample (Fig. 1f). These results indicate that isolated bright spots circled in red represent the Mo SAs anchored on the NiFe LDH support. Notably, the (015) interplanar spacing of the NiFe LDH phase in the LSAMo-NiFe LDH sample is 0.223 nm (Fig. 1g), slightly smaller than the standard value of 0.231 nm. And yet the spacing of the NiFe LDH (110) plane for the LSAMo-NiFe LDH sample (0.153 nm) is already very close to the normal spacing (0.154 nm). HAADF-STEM mapping also shows the uniform distribution of Ni and Fe, and individual spotty distribution of Mo over the entire LSAMo-NiFe LDH sample. This further confirms that the Mo SAs selectively doped into the NiFe LDH (015) facet.

Additionally, to elucidate the metal contents, oxidation states, and electron transfer characteristics, the LSAMo-NiFe LDH sample was analyzed by X-ray photoelectron spectroscopy (XPS). The XPS survey spectra (Fig. S3) verify that the LSAMo-NiFe LDH sample is formed from Fe, C, Mo, Ni, and O elements. The quantitative XPS analysis (Table S1) indicates that the Mo SA content in the LSAMo-NiFe LDH sample is only 0.61 wt%. The high-resolution Ni 2p and Fe 2p spectra of both LDHs were deconvoluted into spin–orbit doublets corresponding to the $2p_{1/2}$ and $2p_{3/2}$ components. The fitted peaks unambiguously confirm the exclusive presence of Ni^{2+} and Fe^{3+} species, respectively.[31,36] Negative binding energy shifts are observed for the LSAMo-NiFe LDH sample, with the Ni $2p_{3/2}$ and Fe $2p_{3/2}$ peaks located at 855.87 and 711.76 eV, corresponding to shifts of 0.27 and 0.22 eV, respectively, compared to the pure NiFe LDH. These shifts confirm electron transfer from Mo SAs to Ni and Fe sites through Mo–O bridging bonds, thereby inducing an electronic rearrangement which in turn enhances the intrinsic OER activity of the NiFe LDH.[31] The O 1s peak at

531.15 eV for the ^{LSA}Mo-NiFe LDH sample, ascribed to the M–OH (M = Ni and Fe) group, exhibits a slightly positive shift of 0.08 eV compared to the pristine NiFe LDH sample (Fig. 2c). This can be attributed to the formation of the Mo–O lattice bond (529.70 eV) and the electron transfer from the lattice oxygen to Mo SAs, which are favorable for lowering the valence state of Mo SAs and optimizing the electron distribution at the Mo SA sites.[37] Furthermore, the Mo 3d spectra (Fig. 2d) are divided into two wide peaks at 228.97 and 231.97 eV, corresponding to the Mo $3d_{5/2}$ and Mo $3d_{3/2}$ doublets, respectively.[30] The binding energy of Mo $3d_{5/2}$ for the ^{LSA}Mo-NiFe LDH sample is slightly less than 229.32 eV for Mo^{III} $3d_{5/2}$ and greater than 228.62 eV for Mo^0 $3d_{5/2}$,[38] illustrating that the chemical valence of Mo SAs for the ^{LSA}Mo-NiFe LDH sample ranges from 0 to +3. These results suggest that Mo SAs have lower valence than high-valent molybdenum oxide (*e.g.*, MoO_2 and MoO_3) reference samples but is never too low and even close to zero. This intermediate oxidation state can be attributed to electronic interactions within the NiFe LDH support, where Ni and Fe act as electron-accepting centers, while lattice oxygen donates electron density, as evidenced by XPS analysis. Instead, if Ni, Fe, and O atoms all act as electron donors within the NiFe LDH support, the resulting electron transfer to the Mo SAs would result in a reduction of the Mo oxidation state, bringing it closer to zero.

To further identify the oxidation state, local atomic structure, and coordination structure of Mo SAs, we carried out X-ray absorption near-edge spectroscopy (XANES) and FT-EXAFS spectra on the ^{LSA}Mo-NiFe LDH electrocatalyst (Fig. 2e–h). The normalized XANES spectra (Fig. 2e) are found by taking the first derivatives with respect to energy, and the Mo K-edge positions of the ^{LSA}Mo-NiFe LDH material and reference samples (*e.g.*, Mo foil, MoO_2, and MoO_3) are determined by the maximum value of the derivative, respectively (Fig. S4). The Mo K-edge absorption energy of ^{LSA}Mo-NiFe LDH (20 015.4 eV) lies between those of Mo foil (20 010.0 eV) and MoO_2 (20 024.5 eV), indicating an average oxidation state of Mo SAs between 0 and +4, which is in good agreement with the XPS results. In view of the function that the absorption edge energy is linearly related to the oxidation state,[39,40] the theoretical fitting (Fig. 2f) further verifies that the average oxidation state of Mo SAs in ^{LSA}Mo-NiFe LDH is as low as +1.9. Furthermore, FT-EXAFS spectra (Fig. 2g) are devoted to revealing and analyzing the local atomic structures and coordination configuration of Mo SAs in the ^{LSA}Mo-NiFe LDH sample, and getting the information of the bond length and coordination numbers between molybdenum and bonding oxygen atoms. Compared to reference samples, the ^{LSA}Mo-NiFe LDH sample exhibits a strong Mo–O scattering peak around 1.32 Å at the first shell but no Mo–Mo bond (2.42 Å), confirming the individual dispersion of Mo SAs and the inexistence of metallic Mo nanoclusters or nanoparticles in ^{LSA}Mo-NiFe LDH, which is in line with the spherical aberration-corrected HAADF-STEM results. The Mo–O bond in the three samples shows different distances (1.32, 1.58, and 1.28 Å), which indicate that the ^{LSA}Mo-NiFe LDH sample does not contain any of molybdenum oxides such as MoO_2 and MoO_3. High-resolution wavelet transform EXAFS (WT-EXAFS) of Mo K-edge for ^{LSA}Mo-NiFe LDH and reference samples also proves the above analysis more intuitively (Fig. 2h). Moreover, the quantitative fittings of FT-EXAFS spectra of Mo K-edge for ^{LSA}Mo-NiFe LDH and all reference samples in *R* space are shown in Fig. S5. Table S2 summarizes the fitting parameters and their reliability can be ensured by the smaller *R* factors. The bond length of Mo–O (1.78 Å) in the ^{LSA}Mo-NiFe LDH sample is shorter than that in MoO_2 (2.02 Å) and MoO_3 (1.85 Å), revealing the higher bond energy of Mo–O in the ^{LSA}Mo-NiFe LDH catalyst. This shortened bond length suggests enhanced bonding strength between Mo single atoms and oxygen, which contributes to improved structural and compositional stability during the oxygen evolution reaction. The average coordination number of Mo–O in ^{LSA}Mo-NiFe LDH is 2.85 ± 0.53, which illustrates that each Mo atom is coordinated with approximately three oxygen atoms, yielding an unsaturated Mo–O_3 electron-rich coordination configuration in the ^{LSA}Mo-NiFe LDH catalyst. These results confirm that low-valent Mo SAs are tightly anchored at the pristine NiFe LDH support by bonding with the oxygen atom with high electronegativity forming the Mo–O_3 configuration.

We then examined how low-valent Mo SAs modulate the inherent OER activity of NiFe LDH. Electrochemical tests were performed at controlled mass loadings using a standard three-electrode system, with catalyst-coated glassy carbon (GC) rotating disk electrode (RDE) as the working electrode in O_2-saturated 1.0 M KOH solution (details in the SI). All polarization curves were *iR*-corrected to account for solution resistance, with validation data provided in Fig. S6. Fig. 3a exhibits the corrected linear scanning voltammetry (LSV) curves swept from high to low potential, from which we discover that the ^{LSA}Mo-NiFe LDH catalyst has smaller overpotential (η_{10}, 228 mV) reached at 10 mA cm^{-2} than pristine NiFe LDH (293 mV) and commercial IrO_2 (331 mV) samples, which indicates that low-valent Mo SAs can significantly reduce the extent of polarization of the ^{LSA}Mo-NiFe LDH modified glassy carbon electrode, making it closer to an equilibrium potential, finally lowering the activation energy barrier during the OER.[41] Remarkably, as Mo SAs are anchored on the NiFe LDH matrix, the Ni^{3+}/Ni^{2+} redox peak (located at 1.335 V *vs.* reversible hydrogen electrode, RHE) moves negatively by 61 mV toward the low potential in comparison to NiFe LDH (1.396 V *vs.* RHE), demonstrating strong electronic coupling between Mo SAs and Ni species that effectively optimizes the electronic structure of ^{LSA}Mo-NiFe LDH, thereby facilitating the interconversion of Ni^{3+}/Ni^{2+}.[42,43] The enhanced peak area can be attributed to the increased concentration of redox-active Ni species, which are effectively activated by the presence of low-valent Mo SAs. This result indicates that the introduction of low-valent Mo single atoms promotes an increased density of catalytically active sites in NiFe LDH.[44] Tafel analysis and electrochemical impedance spectroscopy (EIS) are combined to investigate the role of Mo SAs in OER kinetics. As illustrated in Fig. 3b, the Tafel slope exhibits a significant reduction upon the decoration of Mo SAs, which can be rationally ascribed to the substantial increase in catalytically active sites. The ^{LSA}Mo-NiFe LDH catalyst displays a substantially lower Tafel slope (75.8 mV dec^{-1}) than the pristine NiFe LDH counterpart (118.4 mV dec^{-1}), suggesting the faster reaction kinetics for the OER. EIS spectra (Fig. S7) show

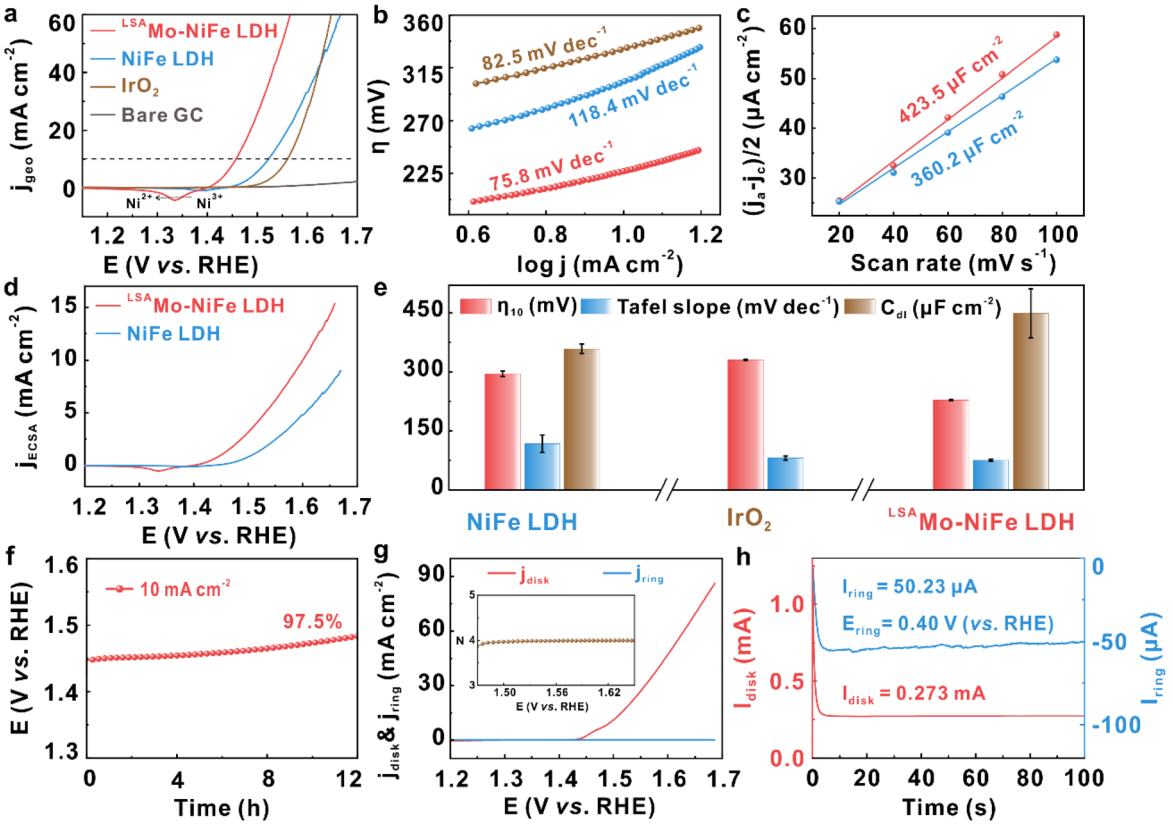

Fig. 3 OER activity of ^{LSA}Mo-NiFe LDH powder in a basic electrolyte. (a) *iR*-corrected LSVs. (b) Tafel plots. (c) C_{dl}. (d) LSVs normalized by ECSA. (e) Standard errors of η_{10}, Tafel slope, and C_{dl} of two LDHs and commercial IrO_2 modified glassy carbon electrodes. (f) Chronopotentiometric stability test of ^{LSA}Mo-NiFe LDH at 10 mA cm^{-2} for 12 h. (g) Disk and ring current densities of ^{LSA}Mo-NiFe LDH recorded during RRDE measurement; the inset illustrates the average number of transferred electrons (*N*) for the OER. (h) Faradaic efficiency measurement of ^{LSA}Mo-NiFe LDH.

a lower charge transfer resistance (R_{ct}) for the ^{LSA}Mo-NiFe LDH catalyst (4.3 Ω, Table S3) compared to pure NiFe LDH without Mo modification, which reveals that the Mo SA decoration effectively facilitates interfacial electron transfer, thereby accelerating the OER kinetics. The electrochemically active surface area (ECSA) is a key index for quantifying accessible active sites participating in the OER at LDH-modified electrode interfaces. We used the cyclic voltammetry (CV) method to measure electrochemical double-layer capacitance (C_{dl}) which is half of the ECSA. The ^{LSA}Mo-NiFe LDH has higher C_{dl} (423.5 μF cm^{-2}) than the pristine counterpart (Fig. 3c), indicating that the anchored Mo SAs effectively introduce Mo sites or activate more Ni or Fe sites for the OER. To decouple geometric effects and accurately evaluate the intrinsic OER activity, the LSV curves and Tafel plots for two LDHs were normalized by their ECSA (Fig. 3d and S8). Even after ECSA normalization, ^{LSA}Mo-NiFe LDH maintains superior activity, exhibiting the lowest overpotential (η_1, 209 mV) and smallest Tafel slope (100.0 mV dec^{-1}) among the tested catalysts, demonstrating that the stabilized Mo SAs significantly enhance the intrinsic OER activity of the NiFe LDH host. To ensure the reliability of the aforementioned OER activity metrics (η_{10}, Tafel slope, and C_{dl}), we conducted multiple tests with at least three independent samples for each LDH. The excellent reproducibility and high reliability of these indicators are clearly evidenced in Fig. 3e and S9. The turnover frequency (TOF) is an important metric for evaluating the intrinsic catalytic activity and was calculated according to the relevant equations (see details in the SI). The ^{LSA}Mo-NiFe LDH catalyst exhibits a TOF of 1.1 s^{-1} at an overpotential of 300 mV, which is significantly higher than that of pristine NiFe LDH (0.6 s^{-1}). This result highlights the enhanced intrinsic activity of ^{LSA}Mo-NiFe LDH.

After elucidating the critical role of Mo SAs in boosting the intrinsic electrocatalytic activity, we further investigated the electrochemical stability of the ^{LSA}Mo-NiFe LDH catalyst and evaluated the average transferred electron number (*N*) and reaction selectivity to gain deeper mechanism insights into its catalytic behavior. Initially, the long-term stability was assessed by galvanostatic testing at a fixed current density of 10 mA cm^{-2}. Fig. 3f exhibits only a marginal overpotential decrease (~2.5%) after 12 h of operation, highlighting its exceptional activity retention. The slight decay is ascribed to the tenuous mechanical adhesion between the ^{LSA}Mo-NiFe LDH powder and the GC substrate: even with Nafion as a binder, prolonged operation still induces partial detachment of the catalyst into the electrolyte. Subsequently, the N and reaction selectivity of ^{LSA}Mo-NiFe LDH for the OER were quantified using rotating RDE (RRDE) measurements (details in the SI). The Pt ring electrode

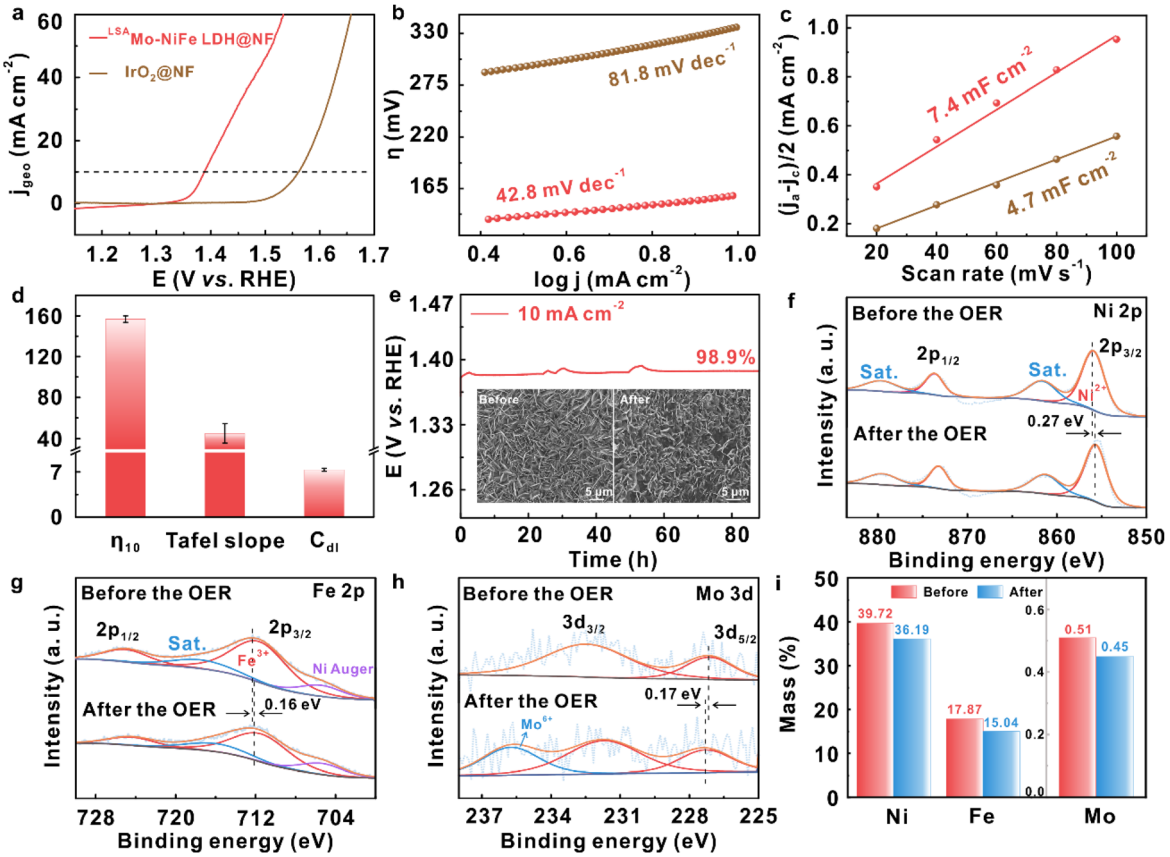

Fig. 4 The overall OER performances and stabilities of the ^{LSA}Mo-NiFe LDH@NF electrode. (a) *iR*-corrected polarization curves. (b) Corresponding Tafel plots. (c) C_{dl}. (d) Standard errors in overpotential at 10 mA cm^{-2} (η_{10}), Tafel slope, and C_{dl}. (e) Chronopotentiometric stability test at 10 mA cm^{-2} for 85 h; the insets show comparative SEM images of the electrode pre-and post-OER testing. High-resolution XPS spectra of (f) Ni 2p, (g) Fe 2p, and (h) Mo 3d regions collected pre-and post-OER stability test. (i) Quantitative elemental analysis of metallic components derived from XPS measurements.

was held at a constant potential of 1.50 V (*vs.* RHE) to ensure complete oxidation of the peroxide intermediate (*e.g.*, OOH^-) generated at the disk electrode. As evidenced in Fig. 3g, the measured ring current (4.29 μA) exhibits a negligible value which is at least three orders of magnitude lower than the disk current (18.2 mA), strongly suggesting the absence of detectable peroxide intermediates during the OER. Quantitative analysis of the ring-disk current ratio yields an N of 3.98 ± 0.02, remarkably close to the ideal four-electron process ($N = 4$), confirming the predominant O_2 generation through an efficient four-electron pathway on the ^{LSA}Mo-NiFe LDH. The reaction selectivity of ^{LSA}Mo-NiFe LDH for catalyzing the OER was quantitatively assessed through Faradaic efficiency (FE) measurement in a N_2-saturated alkaline electrolyte. By applying 0.40 V (*vs.* RHE) to the ring electrode, oxygen generated at the disk electrode was fully reduced *via* the reverse reaction ($2H_2O + O_2 + 2e^- \rightarrow 2OH^- + H_2O_2$), while the N_2 atmosphere prevented dissolved oxygen interference. Calculations based on a disk current of 0.273 mA and ring current of 50.23 μA yielded an ultrahigh FE of 99.5% (Fig. 3h), unambiguously confirming the catalyst's remarkable preference (>99%) for the four-electron water oxidation mechanism ($4OH^- \rightarrow 4e^- + 2H_2O + O_2$) with negligible side reactions.

Building upon the demonstrated intrinsic activity, stability, and selectivity of the two-dimensional (2D) ^{LSA}Mo–NiFe LDH catalyst on a glassy carbon (GC) electrode for the OER, we further sought to enhance mechanical robustness and achieve improved overall, device-relevant performance.[45] To this end, three-dimensional (3D) integrated electrode architecture was developed by directly anchoring ^{LSA}Mo–NiFe LDH onto a conductive nickel foam (NF) scaffold with high surface area, affording a robust, binder-free electrode denoted as ^{LSA}Mo–NiFe LDH @NF. Fig. S10 presents the comprehensive structural and compositional characterization of the ^{LSA}Mo-NiFe LDH@NF electrode through XRD, SEM, and EDS analyses. As shown in Fig. 4a, ^{LSA}Mo–NiFe LDH@NF requires an ultralow overpotential of only 158 mV to reach 10 mA cm^{-2}, which is markedly lower than that of IrO_2/NF. More critically, the Tafel slope of ^{LSA}Mo–NiFe LDH@NF is 42.8 mV dec^{-1}, nearly half that of IrO_2/NF (81.8 mV dec^{-1}) (Fig. 4b). This combination of metrics ranks it among the most active oxygen evolution catalysts reported, particularly in the family of single-atom-modified LDHs (Table S5). The substantially reduced Tafel slope indicates significantly accelerated reaction kinetics and suggests a more favorable rate-determining step with reduced kinetic barriers. In contrast, the larger Tafel slope of IrO_2/NF reflects sluggish

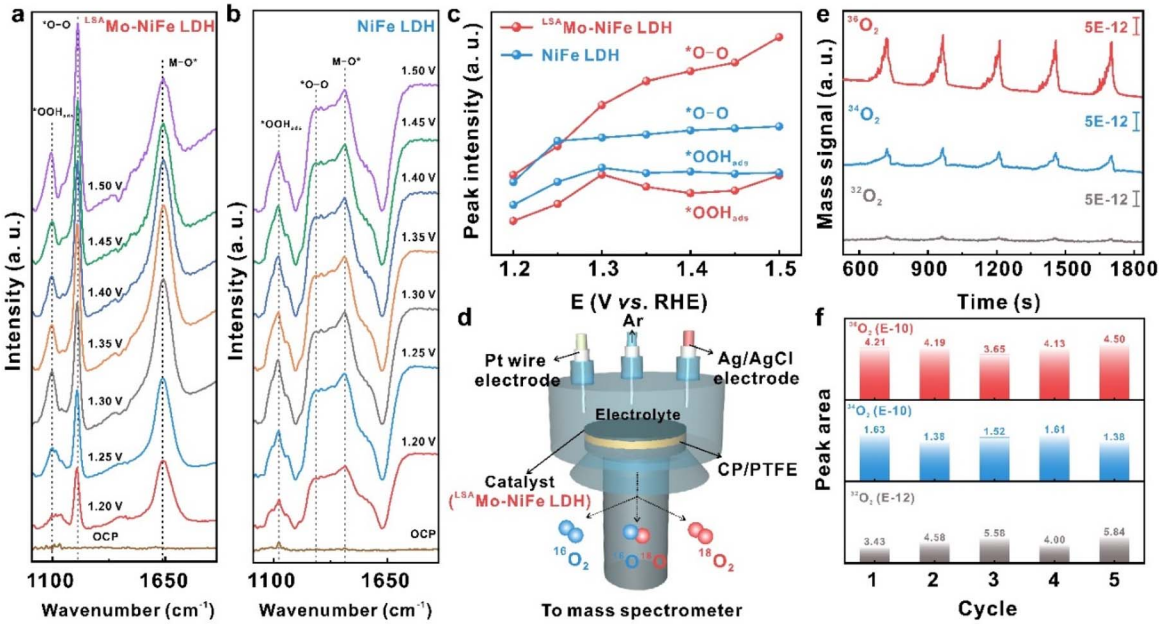

Fig. 5 Mechanistic investigation of the OER pathway on the ^{LSA}Mo-NiFe LDH catalyst through *operando* electrochemical characterization. *Operando* ATR-SEIRAS spectra at different applied potentials for (a) ^{LSA}Mo-NiFe LDH and (b) pristine NiFe LDH. (c) Potential-dependent intensity evolution (1.2–1.5 V *vs.* RHE) of the *O–O and *OOH_{ads} intermediate species. *Operando* DEMS measurements: (d) structural schematic diagram of *operando* DEMS cell configuration. (e) DEMS signals of $^{36}O_2$, $^{34}O_2$, and $^{32}O_2$ for ^{18}O-labeled ^{LSA}Mo-NiFe LDH catalyst in a normal 1.0 M KOH electrolyte. (f) The content of three oxygen products of the ^{18}O-labeled ^{LSA}Mo-NiFe LDH catalyst at each cycle during *operando* DEMS operation.

charge-transfer kinetics and less optimized adsorption energetics of oxygenated intermediates. Furthermore, the 3D NF-supported architecture plays a critical role in performance enhancement. The C_{dl} of ^{LSA}Mo–NiFe LDH@NF reaches 7.4 mF cm^{-2} (Fig. 4c), corresponding to a dramatically enlarged electrochemically active surface area relative to the 2D GC electrode (423.5 μF cm^{-2}). While IrO_2/NF also benefits from the conductive NF scaffold, its comparatively lower capacitive response suggests fewer accessible active sites and/or inferior interfacial charge-transfer characteristics. Fig. 4d also shows the high reproducibility of the OER performance metrics, with minimal deviation across multiple tests. Notably, the 3D electrode exhibits unprecedented long-term stability, maintaining its initial potential at 10 mA cm^{-2} with only 1.1% deviation throughout an 85 h durability test – significantly outperforming the GC-supported counterpart (Fig. 4e). This primarily originates from the robust mechanical coupling between the ^{LSA}Mo-NiFe LDH nanosheets and the NF scaffold. Post-stability characterization using SEM and XPS confirms the retention of both structural integrity and chemical composition in the ^{LSA}Mo-NiFe LDH@NF electrode. As evidenced by the inset in Fig. 4e, the electrode morphology remains essentially unaltered following extended testing, demonstrating remarkable architectural preservation. High-resolution XPS analysis of the post-OER ^{LSA}Mo-NiFe LDH@NF electrode reveals nearly identical spectral profiles for Ni 2p, Fe 2p, and Mo 3d regions (Fig. 4f–h), confirming the structural integrity and stable chemical composition of all metallic constituents throughout the stability test. Further quantitative XPS analyses (Fig. 4i and Table S6) also suggest that each metal element is little etched and corroded in the basic electrolyte during OER operation. Notably, the XPS binding energies of all metallic constituents undergo discernible shifts following stability testing, suggesting reversible redox evolution of their oxidation states during prolonged oxygen evolution operation. Specifically, the Mo 3d peaks shift toward higher binding energies, while the Ni 2p and Fe 2p signals migrate in the opposite direction to lower energies. These observations suggest electron transfer from Mo to neighboring Ni and Fe atoms leading to partial surface oxidation of the ^{LSA}Mo-NiFe LDH structure, which is evidenced by the increased content of high-valent Mo^{6+} cations (235.66 eV) after OER stability measurement. This unique electron transfer stabilizes Ni and Fe against further oxidation under harsh OER conditions, thereby rationalizing the inconsistent oxidation state changes of Ni and Fe observed in previously reported NiFe-based catalysts.[30]

Having established the exceptional OER activity and long-term durability of the ^{LSA}Mo-NiFe LDH@NF electrode, we carried out *operando* electrochemical spectroscopy characterization in tandem with theoretical calculations to elucidate the reaction pathway and mechanism, clarify the contribution of low-valent Mo SAs to the enhanced catalytic performance, as well as identify the rate-determining steps (RDSs) in the OER process. *Operando* ATR-SEIRAS was employed to probe OER-relevant intermediates generated during the electrocatalytic process on both ^{LSA}Mo-NiFe LDH and pristine NiFe LDH catalysts at varying applied potentials (Fig. 5a–c and S11). For ^{LSA}Mo-NiFe LDH (Fig. 5a and S11a), the *operando* ART-SEIRAS spectra display four distinct stretching vibrational bands at 1098, 1223, 1641, and 3165 cm^{-1}, which are assigned to the O–O

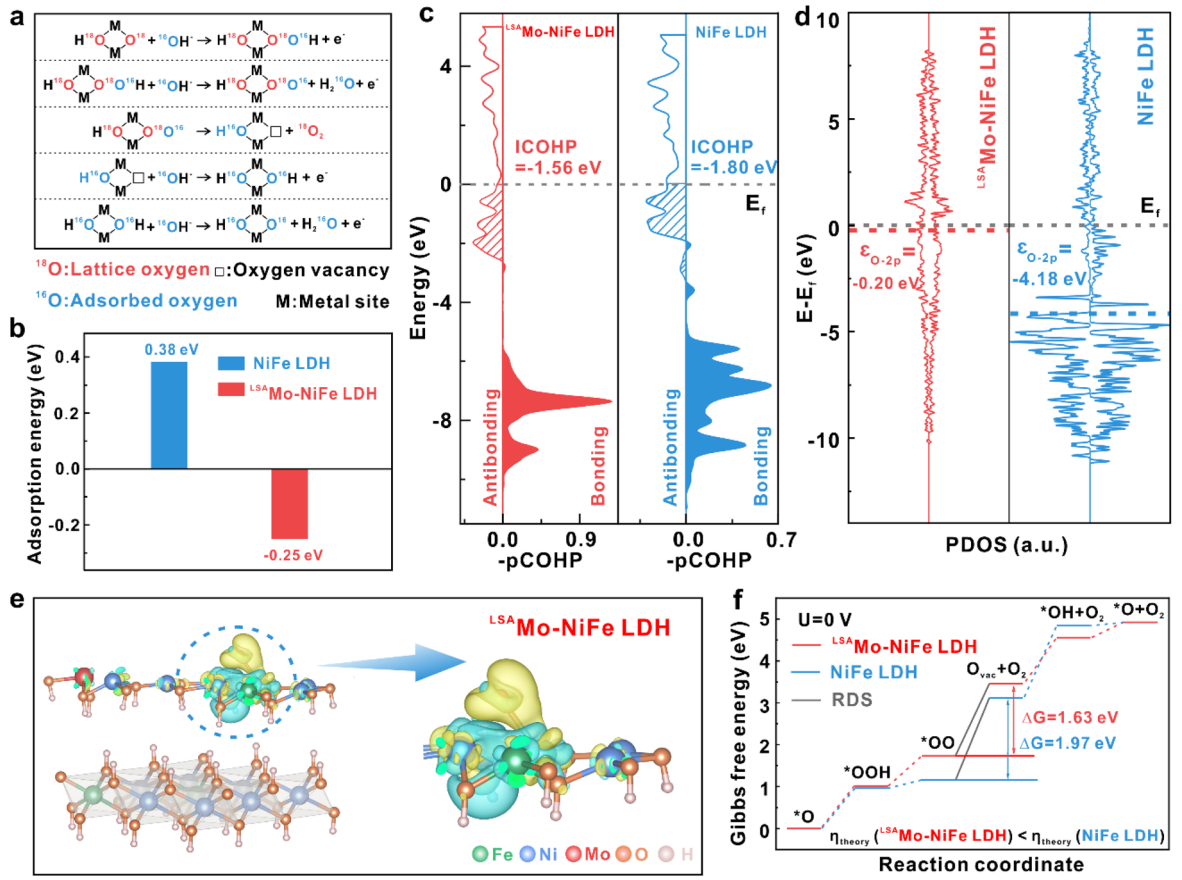

Fig. 6 DFT + *U* investigations reveal the enhanced OER mechanism *via* the lattice oxygen mechanism (LOM) in ^{LSA}Mo-NiFe LDH. (a) Proposed LOM reaction pathway. (b) Calculated OH^- adsorption energies. (c) Projected crystal orbital Hamilton population (pCOHP) analyses of the metal–oxygen bonds. (d) Projected density of states (PDOS) for O 2p orbitals, with the Fermi level aligned at 0 eV. (e) Differential charge density of ^{LSA}Mo-NiFe LDH, where chrome yellow and cyan isosurfaces (set to ±0.004 *e* Bohr^{-3}) represent electron accumulation and depletion, respectively. (f) Gibbs free energy diagrams of the OER.

of adsorbed OOH species (*OOH_{ads}), O–O of *O–O species, the metal–oxygen stretching vibration (M–O*), and O–H of adsorbed hydroxyl species (OH_{ads}), respectively.[46,47] The simultaneous detection of *O–O and *OOH_{ads} intermediates suggests the coexistence of both the lattice oxygen mechanism (LOM) and adsorbate evolution mechanism (AEM) pathways. Crucially, the *O–O peak exhibits significantly higher intensity than *OOH_{ads}, indicating that LOM dominates the OER process on ^{LSA}Mo-NiFe LDH. In contrast, pristine NiFe LDH (Fig. 5b and S11b) also displays similar vibrational bands, with a comparable intensity difference between *O–O and *OOH_{ads}, consistent with literature reports of LOM involvement.[48,49] However, ^{LSA}Mo-NiFe LDH shows a markedly stronger *O–O signal and a substantially weaker *OOH_{ads} signal than NiFe LDH (Fig. 5c), demonstrating that low-valent Mo SA doping facilitates the LOM pathway during OER catalysis. Additionally, the enhanced OH_{ads} signal intensity for ^{LSA}Mo-NiFe LDH (Fig. S11c) indicates stronger hydroxide adsorption and enrichment at oxygen vacancy sites, which arise from lattice oxygen participation in oxygen evolution. This illustrates that low-valent Mo SAs promote lattice oxygen generation, further favoring the LOM-dominated OER pathway.[48] Furthermore, *operando* DEMS coupled with ^{18}O isotope labelling (Fig. 5d) was used to precisely elucidate the OER pathway and mechanism in the case of the ^{LSA}Mo-NiFe LDH catalyst by quantifying the evolution of oxygen isotopologues ($^{32}O_2$, $^{34}O_2$, and $^{36}O_2$). The ^{LSA}Mo-NiFe LDH catalyst was isotopically labeled with ^{18}O through 20 cycles of CV in 1.0 M KOH solution enriched with ^{18}O (details in the SI). As shown in Fig. 5e, mass spectroscopy analysis of the evolved gases during the OER process revealed three distinct oxygen species: $^{36}O_2$ ($^{18}O^{18}O$), $^{34}O_2$ ($^{18}O^{16}O$), and $^{32}O_2$ ($^{16}O^{16}O$). Remarkably, the signal intensity of $^{36}O_2$ surpassed those of $^{34}O_2$ and $^{32}O_2$ by an order of magnitude, respectively. This striking predominance of $^{36}O_2$ unequivocally demonstrates that the oxygen evolution primarily originates from two ^{18}O atoms within the labeled ^{LSA}Mo-NiFe LDH catalyst (Fig. 5f). The detection of $^{34}O_2$ can be explained by the coupling between ^{16}O from the unlabeled alkaline electrolyte and ^{18}O from the labeled catalyst. The overwhelming contribution of $^{36}O_2$ ($^{18}O^{18}O$) provides definitive evidence for lattice oxygen participation in the OER pathway. These results strongly support the conclusion that the OER on ^{LSA}Mo-NiFe LDH proceeds *via* an LOM pathway.

Based on the above identified LOM pathway, we conducted DFT + *U* calculations on the (100) plane of both LDHs to

investigate the role of low-valent Mo SAs and the RDS. As illustrated in Fig. 6a and S12, the LOM proceeds as follows. The nucleophilic attack by $^{16}OH^-$ from the electrolyte on an exposed lattice oxygen (^{18}O) of the ^{18}O labeled LDH forms an $*^{18}O^{16}OH$ intermediate (Step 1). Following this, deprotonation of the intermediate (Step 2) results in the release of gaseous $^{18}O_2$ and the formation of a surface oxygen vacancy (Step 3). The vacancy is subsequently replenished by an oxygen atom (^{16}O) from $^{16}OH^-$ ion in the electrolyte, yielding an ^{16}O labeled LDH surface (Step 4). The cycle concludes with the adsorption and deprotonation of another $^{16}OH^-$ from the electrolyte to regenerate the original metal–oxo species ($M–^{16}O^-$), completing the catalytic cycle (Step 5). The role of low-valent Mo SAs in enhancing OER activity was systematically investigated through three key aspects:

(1) Adsorption energy. The OH^- adsorption energies shown in Fig. 6b reveal a pronounced contrast between ^{LSA}Mo-NiFe LDH (−0.25 eV) and pristine NiFe LDH (0.38 eV), demonstrating a significantly more optimized OH^- binding strength for the ^{LSA}Mo-modified catalyst. This enhanced adsorption behavior is primarily facilitated by the low-valent Mo SAs, which act as favorable adsorption sites for OH^- species. We propose that low-valent Mo SAs effectively capture and subsequently channel OH^- groups to the NiFe LDH matrix, thereby promoting the regeneration of lattice oxygen (Step 4, Fig. 6a) within the LOM process. Moreover, this accelerated regeneration process efficiently mitigates structural degradation that would otherwise result from excessive lattice oxygen evolution.[48]

(2) Bonding interactions and orbital hybridization. The projected crystal orbital Hamilton population (pCOHP) analysis was performed to investigate the metal–oxygen (M–O) bond strength that can represent the OER activity (Fig. 6c). The integrated COHP (ICOHP) was evaluated for occupied states below the Fermi level (E_f), where positive values denote bonding (stabilizing) interactions and negative values represent antibonding (destabilizing) states. Notably, the ICOHP values for the M–O bond are −1.56 eV (^{LSA}Mo-NiFe LDH) and −1.80 eV (pristine NiFe LDH), revealing that Mo SA doping increases electron occupation in antibonding orbitals. This electronic configuration weakens the M–O bond strength, which in turn promotes oxygen vacancy formation and facilitates O_2 release during the LOM process. Furthermore, the O 2p band center (ε_{O-2p}) analysis reveals significant electronic structure modifications induced by low-valent Mo SA doping in NiFe LDH. The ε_{O-2p} exhibits a significant 3.98 eV upward shift from −4.18 eV (pristine NiFe LDH) to −0.20 eV (^{LSA}Mo-NiFe LDH) upon Mo SA incorporation (Fig. 6d), moving closer to the Fermi level—a critical descriptor for OER activity.[49,50] This shift strengthens the hybridization between O 2p states and the Fermi level, which enhances electron depletion from oxygen sites under an anodic potential and promotes lattice oxygen activation. The elevated O 2p band position facilitates deeper Fermi level penetration into the O 2p band, lowering the energy barrier for oxygen vacancy formation and thereby favoring the LOM. These electronic modifications collectively enhance lattice oxygen participation in the OER, demonstrating how Mo SA doping optimizes the catalyst's electronic structure for improved activity.

(3) Electron transfer pathway. Charge density difference analysis (Fig. 6e and S13) demonstrates substantial electron transfer from oxygen atoms to coordinated Mo sites through Mo–O bonds, with partial electron redistribution to neighboring Ni and Fe atoms. This electron redistribution pattern, consistent with XPS results, elucidates the low-valent state of Mo SAs and highlights their role in establishing synergistic electronic interactions within the NiFe LDH matrix. And finally, Gibbs free energy calculations (Fig. 6f) corroborate these findings, showing that the RDS (oxygen vacancy formation) requires a substantially lower theoretical overpotential in ^{LSA}Mo-NiFe LDH (0.40 eV) compared to pristine NiFe LDH (0.64 eV), confirming the crucial role of low-valent Mo SAs in optimizing the OER kinetic pathway.

3 Conclusion

In summary, we have precisely anchored low-valence Mo SAs on the (015) plane of the NiFe LDH matrix (^{LSA}Mo-NiFe LDH) through a solution-phase reductive deposition route. FT-EXAFS analysis conclusively identifies the unique coordination environment of Mo SAs, revealing an unsaturated $Mo–O_3$ configuration that stabilizes electron-rich Mo centers with an exceptionally low average oxidation state (+1.9), and significantly lower than the conventional +4 or +6 states. The as-prepared ^{LSA}Mo-NiFe LDH exhibits extraordinary intrinsic OER activity that outperforms both benchmark NiFe LDH and commercial IrO_2 catalysts, coupled with a Faradaic efficiency of 99.5%. This is due to the synergistic electronic interactions between the low-valence Mo SAs and the NiFe LDH lattice. When assembled into a freestanding electrode on nickel foam (^{LSA}Mo-NiFe LDH@NF), the catalyst demands only 158 mV to reach 10 mA cm^{-2} in 1.0 M KOH, placing it among the top-performing transition metal-based SAC OER electrocatalysts reported to date. Comprehensive post-catalytic characterization studies, including SEM and XPS, confirm the structural integrity and preservation of the low-valent Mo species after prolonged OER operation. Crucially, *operando* ATR-SEIRAS and DEMS studies provide direct evidence that the ^{LSA}Mo-NiFe LDH follows the LOM pathway during OER catalysis. DFT + U calculations demonstrate that low-valent Mo SAs enhance OER activity by optimizing OH^- adsorption energy, facilitating lattice oxygen activation and oxygen vacancy formation, thereby substantially lowering the energy barrier of rate-determining steps. Overall, the present work establishes a general design principle for developing advanced low-valence SACs through the strategic construction of unsaturated coordination environments between transition metal SAs and electronegative oxygen ligands, opening new avenues for the rational design of high-performance OER electrocatalysts.

Author contributions

Yang Yang proposed the research concept, planned and conducted the experiments, prepared the initial draft of the

manuscript, carried out subsequent revisions, and oversaw the overall execution of the project. Ji-Kai Li and Qian-Nan Yang were responsible for catalyst fabrication, material characterization, and electrochemical testing, and they contributed to manuscript preparation. Lin Zhang and Xiao Ma provided support for HAADF-STEM and EELS measurements, as well as the interpretation of the corresponding results. DFT calculations were performed by Yi-Bin Yang, with Jian-Hua Meng and Zhi-Yuan Jiang contributing to the analysis and discussion of the theoretical data. Ying-Dan Wu, Ke-Xiang Wang, Huan Chen, and Rui Chao assisted in the processing and evaluation of experimental results. Wei-Tao Wang and Zhao-Tie Liu contributed to the critical revision and refinement of the manuscript.

Conflicts of interest

The authors declare no conflict of interest.

Data availability

All data can be found in the main article or the supporting information (SI). Supplementary information: experimental details, additional material, and electrochemical characterization data. See DOI: https://doi.org/10.1039/d6sc00877a.

Acknowledgements

This work was financially supported by the National Natural Science Foundation of China (Grant No. 22278261, 22578261, and 52571102), Natural Science Basic Research Program of Shaanxi (No. 2024JC-YBMS-131), and Science and Technology Research Program of Chongqing Municipal Education Commission (Grant No. KJQN202303208).

References

1 W. Z. Zhang, M. H. Liu, X. Gu, Y. X. Shi, Z. F. Deng and N. S. Cai, Water electrolysis toward elevated temperature: advances, challenges and frontiers, *Chem. Rev.*, 2023, **123**(11), 7119–7192, DOI: 10.1021/acs.chemrev.2c00573.

2 Y. W. Dai, J. Yu, J. Wang, Z. P. Shao, D. Q. Guan, Y. C. Huang and M. Ni, Bridging the charge accumulation and high reaction order for high-rate oxygen evolution and long stable Zn-Air batteries, *Adv. Funct. Mater.*, 2022, **24**, 2111989, DOI: 10.1002/adfm.202111989.

3 P. Jovanovič, N. Hodnik, F. Ruiz-Zepeda, I. Arčon, B. Jozinović, M. Zorko, M. Bele, M. Šala, V. S. Šelih, S. Hočevar and M. Gaberšček, Electrochemical dissolution of iridium and iridium oxide particles in acidic media: transmission electron microscopy, electrochemical flow cell coupled to inductively coupled plasma mass spectrometry, and X-ray absorption spectroscopy study, *J. Am. Chem. Soc.*, 2017, **139**(36), 12837–12846, DOI: 10.1021/jacs.7b08071.

4 Y. M. Lee, J. Suntivich, K. J. May, E. E. Perry and Y. Shao-Horn, Synthesis and activities of rutile IrO_2 and RuO_2 nanoparticles for oxygen evolution in acid and alkaline solutions, *J. Phys. Chem. Lett.*, 2012, **3**(3), 399–404, DOI: 10.1021/jz2016507.

5 R. Lang, X. R. Du, Y. K. Huang, X. Z. Jiang, Q. Zhang, Y. L. Guo, K. P. Liu, B. T. Qiao, A. Q. Wang and T. Zhang, Single-atom catalysts based on the metal-oxide interaction, *Chem. Rev.*, 2020, **120**(21), 11986–12043, DOI: 10.1021/acs.chemrev.0c00797.

6 Q. Wang, X. Huang, Z. L. Zhao, M. Y. Wang, B. Xiang, J. Li, Z. X. Feng, H. Xu and M. Gu, Ultrahigh-loading of Ir single atoms on NiO matrix to dramatically enhance oxygen evolution reaction, *J. Am. Chem. Soc.*, 2020, **142**(16), 7425–7433, DOI: 10.1021/jacs.9b12642.

7 P. Kumar, K. Kannimuthu, A. S. Zeraati, S. Roy, X. Wang, X. Y. Wang, S. Samanta, K. A. Miller, M. Molina, D. Trivedi, J. Abed, M. A. C. Mata, H. Al-Mahayni, J. Baltrusaitis, G. Shimizu, Y. A. Wu, A. Seifitokaldani, E. H. Sargent, P. M. Ajayan, J. G. Hu and M. G. Kibria, High-density cobalt single-atom catalysts for enhanced oxygen evolution reaction, *J. Am. Chem. Soc.*, 2023, **145**(14), 8052–8063, DOI: 10.1021/jacs.3c00537.

8 P. Sabatier, *La catalyse en chimie organique*, Hachette Livre, 2019, ISBN: 78-2-329-30377-2.

9 J. K. Nørskov, T. Bligaard, A. Logadottir, S. Bahn, L. B. Hansen, M. Bollinger, H. Bengaard, B. Hammer, Z. Sljivancanin, M. Mavrikakis, Y. Xu, S. Dahl and C. J. H. Jacobsen, Universality in heterogeneous catalysis, *J. Catal.*, 2002, **209**, 275–278, DOI: 10.1006/jcat.2002.3615.

10 J. Y. Cai, X. B. Hao, Z. N. Bian, Y. S. Wu, C. Wei, X. W. Yin, B. Liu, M. Fang, Y. M. Lv, Y. F. Xie, Y. Y Fang and G. M. Wang, Elucidating the discrepancy between the intrinsic structural instability and the apparent catalytic steadiness of M-N-C catalysts toward oxygen evolution reaction, *Angew. Chem., Int. Ed.*, 2024, **63**, e202409079, DOI: 10.1002/anie.202409079.

11 L. F. Yang, Z. T. Ni, Y. F. Zhao, Y. Y. Long, M. Xi, A. R. Chen and H. Zhang, Interfacial electric field stabilized Ru single-atom catalysts for efficient water oxidation, *ACS Catal.*, 2024, **14**, 10820–10828, DOI: 10.1021/acscatal.4c01829.

12 W. M. Haynes, *CRC handbook of chemistry and physics*, CRC Press, 2014, ISBN: 978–1–4822–0867–2.

13 A. P. Freitas, R. F. André, C. Poucin, T. K. Le, J. Imbao, B. Lassalle-Kaiser and S. Carenco, Guidelines for the molybdenum oxidation state and geometry from X-ray absorption spectroscopy at the Mo $L_{2,3}$-edges, *J. Phys. Chem. C*, 2021, **125**(32), 17761–17773, DOI: 10.1021/acs.jpcc.1c01875.

14 H. X. Li, Z. P. Huang, C. F. Zhang, Y. H. Wang, X. Q. Zhang, C. H. Liang and Z. C. Zhang, Affinity descriptor of metal catalysts: concept, measurement and application of oxygen affinity in the catalytic transformation of oxygenates, *Chem. Soc. Rev.*, 2025, **54**, 1905–1923, DOI: 10.1039/D4CS00472H.

15 Y. F. Li, X. Y. Wan, Z. G. Chen, D. Ding, H. Li, N. Zhang, D. Liu and Y. Cui, Activity enhancement of molybdenum carbide in alkaline hydrogen evolution reaction through oxidation-gradient modulation, *ACS Catal.*, 2025, **15**(3), 2270–2281, DOI: 10.1021/acscatal.4c01779.

16 Y. Z. Wu, Y. Y. Zhao, P. L. Zhai, C. Wang, J. F. Gao, L. C. Sun and J. G. Hou, Triggering lattice oxygen activation of single-atomic Mo sites anchored on Ni–Fe oxyhydroxides nanoarrays for electrochemical water oxidation, *Adv. Mater.*, 2022, **29**(34), 2202523, DOI: 10.1002/adma.202202523.

17 Y. Li, T. T. Bo, S. W. Zuo, G. K. Zhang, X. J. Zhao, W. Zhou, X. Wu, G. X. Zhao, H. W. Huang, L. R. Zheng, J. Zhang, H. B. Zhang and J. Zhang, Reversely trapping isolated atoms in high oxidation state for accelerating the oxygen evolution reaction kinetics, *Angew. Chem., Int. Ed.*, 2023, **41**(62), e202309341, DOI: 10.1002/anie.202309341.

18 Z. Chen, F. L. An, Y. Y. Zhang, Z. Y. Liang, W. Y. Liu and M. Y. Xing, Single-atom Mo-Co catalyst with low biotoxicity for sustainable degradation of high-ionization-potential organic pollutants, *Proc. Natl. Acad. Sci. U. S. A.*, 2023, **120**(29), e2305933120, DOI: 10.1073/pnas.2305933120.

19 L. Q. Wang, Z. P. Xu, C. H. Kuo, J. Peng, F. Hu, L. L. Li, H. Y. Chen, J. Z. Wang and S. J. Peng, Stabilizing low-valence single atoms by constructing metalloid tungsten carbide supports for efficient hydrogen oxidation and evolution, *Angew. Chem., Int. Ed.*, 2023, **42**(62), e202311937, DOI: 10.1002/anie.202311937.

20 S. Y. Lu, B. L. Huang, M. Z. Sun, M. C. Luo, M. Jin, H. W. Yang, Q. H. Zhang, H. Liu, P. Zhou, Y. G. Chao, K. Yin, C. S. Shang, J. M. Wang, Y. Wang, F. Lv, L. Gu and S. J. Guo, Synthetic tuning stabilizes a high-valence Ru single site for efficient electrolysis, *Nat. Synth.*, 2024, **3**, 576–585, DOI: 10.1038/s44160-023-00444-x.

21 L. He, M. G. Li, L. Y. Qiu, S. Geng, Y. Q. Liu, F. Y. Tian, M. C. Luo, H. Liu, Y. S. Yu, W. W. Yang and S. J. Guo, Single-atom Mo-tailored high-entropy-alloy ultrathin nanosheets with intrinsic tensile strain enhance electrocatalysis, *Nat. Commun.*, 2024, **15**, 2290, DOI: 10.1038/s41467-024-45874-z.

22 K. A. Moltved and K. P. Kepp, The chemical bond between transition metals and oxygen: electronegativity, d-orbital effects, and oxophilicity as descriptors of metal-oxygen interactions, *J. Phys. Chem. C*, 2019, **123**, 18432–18444, DOI: 10.1021/acs.jpcc.9b04317.

23 C. Tantardini and A. R. Oganov, Thermochemical electronegativities of the elements, *Nat. Commun.*, 2021, **12**, 2087, DOI: 10.1038/s41467-021-22429-0.

24 K. L. Li and D. F. Xue, Estimation of electronegativity values of elements in different valence states, *J. Phys. Chem. A*, 2006, **110**, 11332–11337, DOI: 10.1021/jp062886k.

25 Z. H. Yin, Y. Huang, K. P. Song, T. T. Li, J. Y. Cui, C. Meng, H. G. Zhang and J. J. Wang, Ir single atoms boost metal-oxygen covalency on selenide-derived NiOOH for direct intramolecular oxygen coupling, *J. Am. Chem. Soc.*, 2024, **146**(10), 6846–6855, DOI: 10.1021/jacs.3c13746.

26 H. Mizoguchi and P. M. Woodward, Electronic structure studies of main group oxides possessing edge-sharing octahedra: implications for the design of transparent conducting oxides, *Chem. Mater.*, 2004, **16**(25), 5233–5248, DOI: 10.1021/cm049249w.

27 J. D. Chen, F. Zheng, S. J. Zhang, A. Fisher, Y. Zhou, Z. Y. Wang, Y. Y. Li, B. B. Xu, J. T. Li and S. G. Sun, Interfacial interaction between FeOOH and Ni-Fe LDH to modulate the local electronic structure for enhanced OER electrocatalysis, *ACS Catal.*, 2018, **8**(12), 11342–11351, DOI: 10.1021/acscatal.8b03489.

28 J. X. Kang, X. Y. Qiu, Q. Hu, J. Zhong, X. Gao, R. Huang, C. Z. Wan, L. M. Liu, X. F. Duan and L. Guo, Valence oscillation and dynamic active sites in monolayer NiCo hydroxides for water oxidation, *Nat. Catal.*, 2021, **4**, 1050–1058, DOI: 10.1038/s41929-021-00715-w.

29 M. B. Stevens, C. D. M. Trang, L. J. Enman, J. Deng and S. W. Boettcher, Reactive Fe-sites in Ni/Fe (oxy)hydroxide are responsible for exceptional oxygen electrocatalysis activity, *J. Am. Chem. Soc.*, 2017, **139**(33), 11361–11364, DOI: 10.1021/jacs.7b07117.

30 Y. Jia, X. Ma, Y. B. Yang, R. Chao, J. K. Li, P. F. Guo, B. Zhu, Q. N. Yang, W. T. Wang, L. Liu, Z. T. Liu and Y. Yang, Synthesis, alloying process, and enhanced oxygen evolution activity of highly stable Ni-Fe-Mo nanoparticles with a face-centered cubic phase, *Small*, 2025, e05716, DOI: 10.1002/smll.202505716.

31 Y. Yang, Q. N. Yang, Y. B. Yang, P. F. Guo, W. X. Feng, Y. Jia, K. Wang, W. T. Wang, Z. H. He and Z. T. Liu, Enhancing water oxidation of Ru single atoms via oxygen-coordination bonding with NiFe layered double hydroxide, *ACS Catal.*, 2023, **13**(4), 2771–2779, DOI: 10.1021/acscatal.2c05624.

32 H. G. Yang, C. H. Sun, S. Z. Qiao, J. Zou, G. Liu, S. C. Smith, H. M. Cheng and G. Q. Lu, Anatase TiO_2 single crystals with a large percentage of reactive facets, *Nature*, 2008, **453**, 638–641, DOI: 10.1038/nature06964.

33 X. G. Liu, W. J. Chen, W. Wang, Y. Jiang, K. Z. Cao and Z. B. Jiao, F-regulate the preparation of polyhedral $BiVO_4$ enclosed by high-index facet and enhance its photocatalytic activity, *J. Colloid Interface Sci.*, 2022, **606**, 393–405, DOI: 10.1016/j.jcis.2021.08.023.

34 E. Rutherford, The scattering of α and β particles by matter and the structure of the atom, *Philos. Mag.*, 2012, **92**(4), 669–688, DOI: 10.1080/14786435.2011.617037.

35 S. Yamashita, J. Kikkawa, K. Yanagisawa, T. Nagai, K. Ishizuka and K. Kimoto, Atomic number dependence of Z contrast in scanning transmission electron microscopy, *Sci. Rep.*, 2018, **8**(1), 12325, DOI: 10.1038/s41598-018-30941-5.

36 Y. Yang, L. N. Dang, M. J. Shearer, H. Y. Sheng, W. J. Li, J. Chen, P. Xiao, Y. H. Zhang, R. J. Hamers and S. Jin, Highly active trimetallic NiFeCr layered double hydroxide electrocatalysts for oxygen evolution reaction, *Adv. Energy Mater.*, 2018, **15**(8), 1703189, DOI: 10.1002/aenm.201703189.

37 Y. D. Hu, G. Luo, L. G. Wang, X. K. Liu, Y. T. Qu, Y. S. Zhou, F. Y. Zhou, Z. J. Li, Y. F. Li, T. Yao, C. Xiong, B. Yang, Z. Q. Yu and Y. Wu, Single Ru atoms stabilized by hybrid amorphous/crystalline FeCoNi layered double hydroxide for ultraefficient oxygen evolution, *Adv. Energy Mater.*, 2020, **1**(11), 2002816, DOI: 10.1002/aenm.202002816.

38 T. F. Li, T. Y. Lu, X. Li, L. Xu, Y. W. Zhang, Z. Q. Tian, J. Yang, H. Pang, Y. W. Tang and J. M. Xue, Atomically dispersed Mo

sites anchored on multichannel carbon nanofibers toward superior electrocatalytic hydrogen evolution, *ACS Nano*, 2021, **15**(12), 20032–20041, DOI: 10.1021/acsnano.1c07694.

39 S. P. Cramer, T. K. Eccles, F. W. Kutzler, K. O. Hodgson and L. E. Mortenson, Molybdenum X-ray absorption edge spectra. The chemical state of molybdenum in nitrogenase, *J. Am. Chem. Soc.*, 1976, **98**(5), 1287–1288, DOI: 10.1021/ja00421a053.

40 P. Zimmermann, S. Peredkov, P. M. Abdala, S. DeBeer, M. Tromp, C. Müller and J. A. van Bokhoven, Modern X-ray spectroscopy: XAS and XES in the laboratory, *Coord. Chem. Rev.*, 2020, **423**(15), 213466, DOI: 10.1016/j.ccr.2020.213466.

41 A. J. Bard and L. R. Faulkner, *Electrochemical methods: fundamentals and applications*, John Wiley & Sons, 2001, ISBN: 978−0−471−04372−0.

42 L. Trotochaud, S. L. Young, J. K. Ranney and S. W. Boettcher, Nickel-iron oxyhydroxide oxygen-evolution electrocatalysts: the role of intentional and incidental iron incorporation, *J. Am. Chem. Soc.*, 2014, **136**(18), 6744–6753, DOI: 10.1021/ja502379c.

43 M. W. Louie and A. T. Bell, An investigation of thin-film Ni-Fe oxide catalysts for the electrochemical evolution of oxygen, *J. Am. Chem. Soc.*, 2013, **135**(33), 12329–12337, DOI: 10.1021/ja405351s.

44 X. Yao, E. Halpren, Y. Z. Liu, C. H. Shan, Z. W. Chen, L. X. Chen and C. V. Singh, Intrinsic and external active sites of single-atom catalysts, *iScience*, 2023, **26**, 107275, DOI: 10.1016/j.isci.2023.107275.

45 N. N. Xu, J. A. Wilson, Y. D. Wang, T. S. Su, Y. N. Wei, J. L. Qiao, X. D. Zhou, Y. X. Zhang and S. H. Sun, Flexible self-supported bi-metal electrode as a highly stable carbon- and binder-free cathode for large-scale solid-state zinc-air batteries, *Appl. Catal., B*, 2020, **272**, 118953, DOI: 10.1016/j.apcatb.2020.118953.

46 H. Q. Song, X. Yong, G. I. N. Waterhouse, J. K. Yu, H. Wang, J. M. Cai, Z. Y. Tang, B. Yang, J. W. Chang and S. Y. Lu, RuO_2-CeO_2 lattice matching strategy enables robust water oxidation electrocatalysis in acidic media via two distinct oxygen evolution mechanisms, *ACS Catal.*, 2024, **14**(5), 3298–3307, DOI: 10.1021/acscatal.3c06182.

47 Y. Hu, Y. Zheng, J. Jin, Y. T. Wang, Y. Peng, J. Yin, W. Shen, Y. C. Hou, L. Zhu, L. An, M. Lu, P. X. Xi and C. H. Yan, Understanding the sulphur-oxygen exchange process of metal sulphides prior to oxygen evolution reaction, *Nat. Commun.*, 2023, **14**(1), 1949, DOI: 10.1038/s41467-023-37751-y.

48 F. Y. Wu, F. Y. Tian, M. G. Li, S. Geng, L. Y. Qiu, L. He, L. L. Li, Z. Y. Chen, Y. S. Yu, W. W. Yang and Y. L. Hou, Engineering lattice oxygen regeneration of NiFe layered double hydroxide enhances oxygen evolution catalysis durability, *Angew. Chem., Int. Ed.*, 2025, **1**(64), e202413250, DOI: 10.1002/anie.202413250.

49 Z. Y. He, J. Zhang, Z. H. Gong, H. Lei, D. Zhou, N. Zhang, W. J. Mai, S. J. Zhao and Y. Chen, Activating lattice oxygen in NiFe-based (oxy)hydroxide for water electrolysis, *Nat. Commun.*, 2022, **13**, 2191, DOI: 10.1038/s41467-022-29875-4.

50 Y. M. Sun, H. B. Liao, J. R. Wang, B. Chen, S. N. Sun, S. J. H. Ong, S. B. Xi, C. Z. Diao, Y. H. Du, J. O. Wang, M. B. H. Breese, S. Z. Li, H. Zhang and Z. C. J. Xu, Covalency competition dominates the water oxidation structure-activity relationship on spinel oxides, *Nat. Catal.*, 2020, **3**(7), 554–563, DOI: 10.1038/s41929-020-0465-6.